Title

Application of a partially relaxed shape memory free energy function to bound the phase diagram and predict global microstructure evolution

Authors

Hall, Garrett
Govindjee, Sanjay

Publication Date

2000-11-01

Report No.
UCB/SEMM-2000/09

Structural Engineering
Mechanics and Materials

Application of a Partially Relaxed Shape Memory Free Energy Function to Bound the Phase Diagram and Predict Global Microstructure Evolution

By

Garrett J. Hall

and

Sanjay Govindjee

November 2000

Department of Civil and Environmental Engineering
University of California, Berkeley

Application of a Partially Relaxed Shape Memory Free Energy Function to Bound the Phase Diagram and Predict Global Microstructure Evolution

Garrett J. Hall[a] and Sanjay Govindjee[a]

[a]Structural Engineering, Mechanics, and Materials
Department of Civil and Environmental Engineering
University of California, Berkeley
Berkeley, CA 94720-1710

November 21, 2000

ABSTRACT

In this work recent results regarding bounds of the relaxed free energy functions of a broad class of shape memory materials of arbitrary symmetry are leveraged to develop a simple and efficient numerical method to analyze several aspects of the thermomechanical response of such materials. This approach is shown to be useful for construction of the austenitic phase diagram used in many early phenomenological models. It is also demonstrated that the resulting implementation is suitable for finite element analysis, has desirable numerical properties, and makes realistic quantitative predictions regarding the evolution of the lattice correspondence variants, transformation stress and strain levels, and orientation dependence.

Keywords: Shape Memory Alloys, Phase Transformation, Constitutive Behavior

Further author information:
S.G.: E-mail: govindjee@ce.berkeley.edu
G.J.H.: E-mail: gjhall@ce.berkeley.edu

1. INTRODUCTION

The class of materials generically referred to as shape memory alloys have the unique ability to undergo reversible phase transformation and reversible martensitic reorientation when subjected to appropriate mechanical and thermal loads. These properties have led to an ongoing proliferation of commercial and industrial applications which, at least initially, outpaced the development of adequate mathematical theories from which to rigorously interpret the observed behavior. However, the gap between engineering applications and the ability to predict apriori the material response has closed considerably with the ongoing development of models ranging from the phenomenological to the purely theoretical (see, for example, Gurtin (1983), Achenbach & Müller (1985), Ball & James (1987), Kohn (1991), Brinson & Lammering (1993), Abeyaratne, Kim & Knowles (1994), Boyd & Lagoudas (1996), Huang & Brinson (1998), Govindjee & Kasper (1999), Siredey, Patoor, Berveiller & Eberhardt (1999), Qidwai & Lagoudas (2000), Bhattacharya & Dolzmann (2000) and Mielke & Kuczma & Theil (1998) to name a few). In recent years, the two modeling extremes have narrowed in a convergence towards a theoretically consistent framework incorporating a mathematical description of the underlying microstructure.

Continuing the line of research efforts this paper demonstrates that the partially relaxed free energy function which arises in the analysis of optimal microstructures can be exploited to provide a convenient and efficient method for predicting the spatial variation of microstructure for arbitrary boundary value problems. Through the use of an approximate relaxed energy functional recently investigated by Govindjee & Mielke (2000), this work extends a similar approach taken by Carstensen (1997) and Carstensen (2000) for the two-well problem to the multi-well problem and connects it to the phase space approach (see e.g. Xiaochuang & Pence (1998)). It is shown that only minimal information regarding the lattice correspondent variants is required to obtain results which match surprisingly well with experimental observations, both in terms of the microstructure evolution and the stress transformation response, despite the simplicity of the formulation. Experimental comparison is made to the work of Shield (1995).

1.1. Theoretical Background

Typical shape memory alloys are known to transform between two solid phases which are distinguished by the point symmetry group of the crystalline lattice in each state. The most commonly available crystals and polycrystals of this type have a high temperature lattice (austenite) of greater symmetry than the lower temperature (martensite) lattice. For most symmetry transformations, the diffusionless transformation from austenite to martensite is necessarily nonunique due to the fact that there are multiple equivalent orientations of the lower symmetry lattice with respect to the parent lattice. Each orientation of the martensite lattice is referred to as a variant, or more specifically, a lattice correspondent variant. It is well known that if one defines the point group of a crystal as the set of rotations that map a given lattice back into itself, then the ratio of the order of the higher symmetry point group $\mathcal{P}_a$ to the order of the lower symmetry point $\mathcal{P}_m$ group gives the number of equivalent transformations (Ericksen 1989). For example, one would expect that a cubic $\leftrightarrow$ orthorhombic phase change would produce $\mathrm{O}(\mathcal{P}_a)/\mathrm{O}(\mathcal{P}_m) = 24/4 = 6$ lattice correspondent variants of martensite.

With this in mind, consider a reference configuration of a bounded deformable body occupying a region $\Omega_o \subset \mathbb{R}^3$ which is acted on by the regular mapping $\varphi^\alpha : \Omega_o \to \Omega \subset \mathbb{R}^3$ which takes points

in the reference body to the spatial configuration $\boldsymbol{x} = \boldsymbol{\varphi}^\alpha(X)$. $\boldsymbol{\varphi}^\alpha$ represents the point mapping associated with a symmetry change from austenite to martensitic variant α. Using this framework, each martensitic variant may be associated with a measurable deformation $\boldsymbol{F}^\alpha = \mathrm{GRAD}(\boldsymbol{\varphi}^\alpha)$ and hence a strain which occurs in the transformation between austenite and martensite . These strains, as measured (for example) by the Green Lagrange tensors $\boldsymbol{E}^\alpha = \frac{1}{2}(\boldsymbol{F}^{\alpha^T}\boldsymbol{F}^\alpha - \mathbf{1})$, relate the lattice parameters of the two phases and are symmetry related via the austenite point group of the material at hand. The values of these strains, sometimes known as Bain strains, are widely reported in the literature; see e.g. Nenno & Saburi (1981) or Bhattacharya & Kohn (1996).

If we assume the existence of a free energy density for our material in the form $W = \hat{W}(\boldsymbol{E}, \theta)$ where $\boldsymbol{E}$ is the Green Lagrange strain of the material and θ is the temperature, then it is clear that the nature of the phase transition places restrictions on the form of the free energy. In addition to Galilean invariance, which is easily satisfied by taking W a function of $\boldsymbol{E}$, the material must be invariant with respect to the underlying material symmetry. Since the martensitic variants are identical in every way save orientation, the resulting function must have multiple "wells" corresponding with austenite and each variant of martensite (Ball & James 1987). At the transition temperature and under strain free conditions, every local minimum is required to be equal; this may be taken as a definition for the transition temperature. However, the critical feature to note is that the energy W, hereafter referred to as the microstructural energy, is intrinsically non-convex. Two such examples are Landau's polynomial approximation, see Ericksen (1986), and

$$W = \min_\alpha \{W^\alpha\}, \tag{1}$$

(Kohn 1991), where W^α is the free energy of an elastic system centered on each well α.

Assuming for the moment that W may be specified or at least approximated, the question then arises as to how a body made of such a material will evolve under a given set of boundary conditions. Treating it as an equilibrium problem, it is reasonable to investigate solutions which minimize the free energy for the body

$$E \equiv \inf_{\boldsymbol{v}} \left\{ \int_{\Omega_o} W(\boldsymbol{E}(\boldsymbol{v}), \theta) \mathrm{dV} \right\} \tag{2}$$

over sufficiently smooth displacement fields $\boldsymbol{v}$ satisfying the boundary conditions on $\partial\Omega_o$. This has been the subject of numerous works by Ball & James (1987), Ball & James (1992), Gurtin (1983), and Bhattacharya (1993), among many others. Unfortunately, comprehensive solution strategies have proved elusive as in general the minimizing sequences oscillate at finer and finer scales, never obtaining the infimum. While this is consistent with the development of fine scale microstructure observed in experiments, it does not provide the tools necessary to analyze arbitrary geometries and boundary conditions, nor does it lead to stable numerical techniques for making such predictions.

In response to this deficiency, much work has been aimed at developing *relaxed* free energy functions (Dacorogna 1989), that is, the associated quasiconvex function defined by

$$QW(\boldsymbol{F}, \theta) \equiv \inf_{\boldsymbol{v}} \left\{ \frac{\int_{\Omega_o} W(\boldsymbol{E}(\boldsymbol{v}), \theta) \mathrm{dV}}{\int_{\Omega_o} \mathrm{dV}} \;\middle|\; \boldsymbol{v} = \boldsymbol{F}\boldsymbol{X} \;,\; \boldsymbol{X} \in \partial\Omega_o \right\} \tag{3}$$

where again $\boldsymbol{v}$ is sufficiently smooth and satisfies the boundary conditions on $\partial\Omega_o$. This approach, which requires the microstructural free energy function, has been applied to the linearized two-well

problem (Kohn 1991) and more recently the three well problem (Smyshlyaev & Willis 1999). This is significant in that the minimum to the relaxed problem

$$E_r = \inf_{\boldsymbol{v}} \left\{ \int_{\Omega_o} QW(\boldsymbol{F}(\boldsymbol{v}), \theta) \mathrm{dV} \right\} \tag{4}$$

has as its solution the infimum of the microstructural free energy, $E = E_r$, and moreover always obtains its infimum. As such, its predicts the correct phase and variant volume fractions albeit without determining the precise microstructural pattern. The primary drawback to this approach is that exact solutions have proven elusive with the notable exceptions of the linearized two and three well problems in the special case of equal elastic moduli at each well.

Recently two approaches have been proposed for circumventing the difficulty in deriving expressions for the relaxed energy. The first, proposed by Bhattacharya & Dolzmann (2000), is to construct functions which satisfy the essential properties of the relaxed free energy directly without appealing to the microstructural density. Although it is not clear if the method is applicable to more general problems, the technique has been demonstrated for two-dimensional instances of two and four well problems. The second approach, which will be followed here, is motivated by an equivalent statement of Eq.(3) for the linearized case

$$QW(\boldsymbol{\varepsilon}, \theta) \equiv \inf_{\boldsymbol{\tau}} \inf_{\boldsymbol{v}} \left\{ \frac{\int_{\Omega_o} \sum_{\alpha}^{nv+1} \tau^{\alpha} W^{\alpha}(\boldsymbol{\varepsilon} + \boldsymbol{\epsilon}(\boldsymbol{v}), \theta) \mathrm{dV}}{\int_{\Omega_o} \mathrm{dV}} \right\} \tag{5}$$

where $\boldsymbol{\varepsilon}$ and $\boldsymbol{\epsilon}$ are small strain measures, W^{α} is the free energy function of variant α, $\boldsymbol{\tau} \in \mathbb{R}^{nv+1}$ is a vector of the $nv+1$ phase variant indicator functions $\tau^{\alpha}(\boldsymbol{X}) \in \{0, 1\}$, and θ is a fixed temperature value. Stated in this form, one may define the partially relaxed free energy function $Q_{\xi}W$ as the optimal microstructural arrangement under fixed volume fractions ξ^{α} (Kohn 1991). Using notation common in the literature, the function

$$Q_{\xi}W(\boldsymbol{\varepsilon}, \theta, \boldsymbol{\xi}) \equiv \inf_{\boldsymbol{\tau}} \inf_{\boldsymbol{v}} \left\{ \frac{\int_{\Omega_o} \sum_{\alpha}^{nv+1} \tau^{\alpha} W^{\alpha}(\boldsymbol{\varepsilon} + \boldsymbol{\epsilon}(\boldsymbol{v}), \theta) \mathrm{dV}}{\int_{\Omega_o} \mathrm{dV}} \;\middle|\; \xi^{\alpha} = \frac{\int_{\Omega_o} \tau^{\alpha} \mathrm{dV}}{\int_{\Omega_o} \mathrm{dV}} \right\} \tag{6}$$

is related to the relaxed free energy via

$$QW(\boldsymbol{\varepsilon}, \theta) = \inf_{\boldsymbol{\xi}} \{ Q_{\xi}W(\boldsymbol{\varepsilon}, \theta, \boldsymbol{\xi}) \} \tag{7}$$

where the volume fractions naturally sum to one and are non-negative. In the two well problem Kohn derived exact expressions for both the partially relaxed $Q_{\xi}W$ and fully relaxed QW functions for the case $nv+1 = 2$, whereas Smyshlyaev & Willis (1999) investigated the case $nv+1 = 3$. Recently Govindjee & Mielke (2000) have extended this approach by deriving bounds for the partially relaxed free energy for a problem with an arbitrary number of phase variants; the resulting partially relaxed free energy functions will be used here.

In what follows, the partially relaxed free energy of Govindjee and Mielke is exploited to simulate the evolution of microstructure as well as the idealized mechanical response for a typical shape memory alloy. The approach taken, which is similar to that employed by Carstensen (2000) for

Kohn's two well problem, is shown to result in a particularly simple and stable numerical implementation. Although no treatment of the kinetics or hysteresis exhibited by shape memory alloys is included, the effectiveness of the method for capturing the quantitative response of such materials is demonstrated by comparison with experimental data.

An outline of the remainder of the paper is as follows. In Section 2 the aforementioned partially relaxed free energy is presented in a continuum setting along with its associated constrained potential which takes into account mass conservation explicitly. This is followed in Section 3 by a discussion of transformation surfaces, often referred to as "yield" surfaces in the literature (see e.g. Huang (1999)) which are noted to have a transparent physical interpretation and allow for effective determination of the phase state. Section 4 then outlines the methodology required to employ the model in a discrete setting, with attention paid to the numerical issues surrounding the implementation. The stability, global convergence, and correspondence with experimental data are investigated in Section 5 by solving a series of three dimensional boundary value problems numerically. In closure, Section 6 offers some concluding remarks.

2. MODEL EQUATIONS

In this section the continuum constitutive equations are presented. The fundamental structure is given by the statement of the free energy and its associated Lagrangian potential under the constraint of mass conservation. The second essential component is the specification of an evolution law for the phase fractions, which in this case is posed as the solution to an optimization problem. Once this rule is established to govern the internal variables in the free energy statement, the system is closed and the remaining task is to examine the consequences of the above choices, e.g. the stress function and the thermodynamic properties of the postulated material.

2.1. Energetic Structure

Consistent with Eq.(1), the first step is to specify the elastic free energy functions centered on each of the $nv + 1$ minima of the microstructural energy. As a matter of notational convenience the set of phase variants will be denoted by $\mathcal{S}$ where, for example, $\mathcal{S} = \{a, m_1, m_2, m_3\}$ for a cubic $\leftrightarrow$ tetragonal material which has an austenite phase and three lattice correspondent variants of the martensitic phase. Then, taking as arguments the linearized strain measure $\boldsymbol{\varepsilon} \in \mathbb{S}^3$ and the absolute temperature θ, the simplest choice is a classical thermoelastic material. Denoting the purely thermal terms by υ^α and the thermomechanical terms by χ^α, the free energy function of each crystallographic variant is given by

$$\hat{\psi}^\alpha(\boldsymbol{\varepsilon}, \theta) = \hat{\chi}^\alpha(\boldsymbol{\varepsilon}, \theta) + \hat{\upsilon}^\alpha(\theta). \tag{8}$$

The first of these functions is specified as

$$\chi^\alpha = \frac{1}{2}(\boldsymbol{\varepsilon} - \boldsymbol{\varepsilon}^{\alpha_t} - \Delta\theta\boldsymbol{\varepsilon}^{\alpha_\theta}) : \mathbb{C} : (\boldsymbol{\varepsilon} - \boldsymbol{\varepsilon}^{\alpha_t} - \Delta\theta\boldsymbol{\varepsilon}^{\alpha_\theta}) \tag{9}$$

where $\Delta\theta = \theta - \theta_o$ is the distance from the reference temperature θ_o, $\boldsymbol{\varepsilon}^{\alpha_\theta}$ is the thermal expansion structural tensor, and $\boldsymbol{\varepsilon}^{\alpha_t}$ is the Bain strain. The notation (:) has its usual interpretation as the double contraction, in this case between rank-2 and rank-4 tensors in $\mathbb{R}^3$. Also note that each

variant is assumed to have the same rank-4 elasticity tensor $\mathbb{C}$, which hereafter will be assumed to be isotropic. The thermal function is the same one used by Abeyaratne, Kim & Knowles (1994) where it is assumed that austenite and martensite have the same mass density ρ and heat capacity c:

$$\upsilon^\alpha = \rho_o c\theta(1 - \log(\theta/\theta_o)) - \rho_o\lambda^\alpha(1 - \theta/\theta_o) - \frac{1}{2}(\Delta\theta)^2\boldsymbol{\varepsilon}^{\alpha_\theta}:\mathbb{C}:\boldsymbol{\varepsilon}^{\alpha_\theta}. \tag{10}$$

Note that λ^α is the latent heat of transformation, which by crystallographic symmetry must satisfy

$$\lambda^\alpha = \lambda^\beta \quad \forall \quad \alpha, \beta \in \{\mathcal{S} \setminus a\}. \tag{11}$$

With this choice of microstructural energy, $W = \min_{\alpha\in\mathcal{S}}\{\psi^\alpha\}$. The next step is to relax the free energy with respect to the microstructural arrangement under fixed temperature and volume fractions in the manner implied by Eq.(6). The solution naturally decouples into the terms (Kohn 1991)

$$Q_\xi W = \sum_{\alpha\in\mathcal{S}} \xi^\alpha\psi^\alpha + \hat{\Psi}^{\mathrm{M}}(\boldsymbol{\xi}) \tag{12}$$

where $\hat{\Psi}^{\mathrm{M}}$ is a convex function of the volume fractions typically referred to as the free energy of mixing. While no closed form solution is known for the general $nv + 1$ case, Govindjee & Mielke (2000) have derived a bound which is exact for a large subset of the domain of $\boldsymbol{\xi}$. This is restated here as

$$Q_\xi W \approx \boldsymbol{\xi}\cdot\boldsymbol{\psi} + \hat{\Psi}^{\mathrm{M}}_{\text{Reuß}}(\boldsymbol{\xi}) \tag{13}$$

where $\Psi^M_{\text{Reuß}}$ is a lower bound to the exact energy of mixing ($\Psi^{\mathrm{M}} \geq \Psi^{\mathrm{M}}_{\text{Reuß}}$). The first term of Eq.(13) is equivalent to the first term in Eq.(12) with the free energy and volume fractions expressed in vector notation using the standard orthonormal basis so that $\boldsymbol{\xi}, \boldsymbol{\psi} \in \mathbb{R}^{nv+1}$ and $(\cdot)$ is the usual inner product. This notation is convenient as the mixture energy can be expressed as

$$\Psi^{\mathrm{M}}_{\text{Reuß}} = \frac{1}{2}\boldsymbol{\xi}\cdot\boldsymbol{\Phi}\cdot\boldsymbol{\xi} - \frac{1}{2}\boldsymbol{\xi}\cdot\boldsymbol{\phi} \tag{14}$$

where the $\boldsymbol{\Phi}$ and $\boldsymbol{\phi}$ are a matrix and a vector of interaction terms respectively. They are related by

$$\boldsymbol{\phi} = \mathrm{diag}(\boldsymbol{\Phi}) \tag{15}$$

where $\mathrm{diag}(\cdot)$ implies that $\phi^\alpha = \Phi^{\alpha\alpha}$ for all $\alpha \in \mathcal{S}$ (no summation). Anticipating details of the implementation, it will prove convenient to further separate the mechanical, thermomechanical, and thermal terms as

$$\boldsymbol{\Phi} = \boldsymbol{\Phi}_{tt} + (\Delta\theta)\boldsymbol{\Phi}_{t\theta} + (\Delta\theta)^2\boldsymbol{\Phi}_{\theta\theta} \tag{16}$$

where the entries of each matrix are

$$\Phi^{\alpha\beta}_{tt} = \boldsymbol{\varepsilon}^{\alpha_t}:\mathbb{C}:\boldsymbol{\varepsilon}^{\beta_t} \tag{17}$$

$$\Phi^{\alpha\beta}_{t\theta} = \boldsymbol{\varepsilon}^{\alpha_t}:\mathbb{C}:\boldsymbol{\varepsilon}^{\beta_\theta} + \boldsymbol{\varepsilon}^{\beta_t}:\mathbb{C}:\boldsymbol{\varepsilon}^{\alpha_\theta} \tag{18}$$

$$\Phi^{\alpha\beta}_{\theta\theta} = \boldsymbol{\varepsilon}^{\alpha_\theta}:\mathbb{C}:\boldsymbol{\varepsilon}^{\beta_\theta}. \tag{19}$$

Since these three matrices depend upon only the Bain strain and the structural part of the thermal expansion strain, they are constants under changes in strain or temperature and as such need only

be computed once. It is also worth noting that although Φ is symmetric, it is at best semi-definite. To see this, consider a situation at the reference temperature and recall that the minimum of the austenite well is strain free. This point will be returned to shortly.

With the definitions given in Eq.'s(15-19), a statement of the partially relaxed free energy which coincides with Eq.(6) is given by

$$Q_\xi W \equiv \boldsymbol{\xi}\cdot\boldsymbol{\psi} - \frac{1}{2}\boldsymbol{\xi}\cdot\boldsymbol{\phi} + \frac{1}{2}\boldsymbol{\xi}\cdot\boldsymbol{\Phi}\cdot\boldsymbol{\xi}. \tag{20}$$

This relation is constrained by the restrictions

$$\sum_{\alpha\in\mathcal{S}} \xi^\alpha = 1 \tag{21}$$

$$\xi^\alpha \geq 0 \ \forall\, \alpha \in \mathcal{S} \tag{22}$$

Following the approach used by several authors (Siredey et al. (1999), Huang & Brinson (1998)) it is useful to explicitly include the volume fraction constraints in the free energy by constructing the corresponding Lagrangian potential. The result is the free energy of Govindjee & Miehe (2000) in which the first constraint is written as $\boldsymbol{\xi}\cdot\boldsymbol{e}^* - 1 = 0$ so that

$$\Psi \equiv \boldsymbol{\xi}\cdot\boldsymbol{\psi} - \frac{1}{2}\boldsymbol{\xi}\cdot\boldsymbol{\phi} + \frac{1}{2}\boldsymbol{\xi}\cdot\boldsymbol{\Phi}\cdot\boldsymbol{\xi} + \delta(\boldsymbol{\xi}\cdot\boldsymbol{e}^* - 1) - \boldsymbol{\gamma}\cdot\boldsymbol{\xi} \tag{23}$$

where $\boldsymbol{e}^* \in \mathbb{R}^{nv+1}$ is a vector of ones in the standard orthonormal basis. The Lagrange multipliers are δ and $\boldsymbol{\gamma}$, the second of which satisfies the Kuhn-Tucker conditions $\boldsymbol{\gamma}\cdot\boldsymbol{\xi} = 0$ and $\gamma^\alpha \geq 0$ (see Govindjee & Miehe (2000) for a complete discussion). In what follows, Eq.(23) will serve as the free energy of the material. The determination of the internal variable $\boldsymbol{\xi}$ is discussed next.

2.2. Relaxed Free Energy

Taking Ψ to be the approximate partially relaxed free energy, the approximate quasiconvex free energy is obtained through an optimization over the space of volume fractions. In light of the previous section, Eq.(7) becomes

$$\widehat{QW}(\boldsymbol{\varepsilon},\theta) = \inf_{\boldsymbol{\xi}} \left\{ \hat{\Psi}(\boldsymbol{\varepsilon},\theta,\boldsymbol{\xi}) \right\} \tag{24}$$

which explicitly includes the balance of mass constraints. By solving this problem for a given strain and temperature, the average volume fractions are determined. Thus, Eq.(24) serves as the state determination law for the phase fractions which can be thought of as the internal variable of the system. In this section the optimality conditions which govern a solution to Eq.(24) are outlined; numerical issues associated with finding the solution are covered in Section 4.

Although the problem as stated is an inequality constrained problem in the variables $\boldsymbol{\xi}$, it is possible to convert it to an equality constrained problem through the use of an active set strategy. To that end, it is assumed that a set $\mathcal{C}$ is maintained which lists the active constraints. Keeping this in mind, the first order optimality conditions for the reduced equality problem are

$$\boldsymbol{0} = \boldsymbol{\psi} - \frac{1}{2}\boldsymbol{\phi} + \boldsymbol{\Phi}\cdot\boldsymbol{\xi} + \delta\boldsymbol{e}^* - \boldsymbol{\gamma} \tag{25}$$

$$0 = \boldsymbol{\xi}\cdot\boldsymbol{e}^* - 1 \tag{26}$$

$$0 = -\xi^\alpha \ , \ \alpha \in \mathcal{C}. \tag{27}$$

In order to rewrite these equations in a more convenient form, we define $\bar{\gamma}$ implicitly through

$$\gamma^\alpha = \begin{cases} 0 & \alpha \in \{\mathcal{S} \setminus \mathcal{C}\} \\ \bar{\gamma}^\alpha & \alpha \in \mathcal{C}. \end{cases} \tag{28}$$

It should be noted that it is not possible to have all of the inequality constraints active, $\mathcal{C} \neq \mathcal{S}$, as it would contradict the equality constraint. In the context of optimization, this is consistent with the notion that the constraints in the active set should be linearly independent. This can be seen by writing the above set of equations in the matrix form

$$\begin{Bmatrix} \frac{1}{2}\phi - \psi \\ 1 \\ 0 \end{Bmatrix} = \begin{bmatrix} \Phi & e^* & -\mathbb{I}_\mathcal{C} \\ (e^*)^T & 0 & 0 \\ -\mathbb{I}_\mathcal{C}^T & 0 & 0 \end{bmatrix} \begin{Bmatrix} \xi \\ \delta \\ \bar{\gamma} \end{Bmatrix} \tag{29}$$

where if $\dim(\mathcal{C}) = m$ then $\bar{\gamma} \in \mathbb{R}^m$ is the vector containing only the active elements of γ and $\mathbb{I}_\mathcal{C} \in \mathbb{R}^{(nv+1)\times m}$ is defined such that $\mathbb{I}_\mathcal{C}\bar{\gamma} = \gamma$. In other words, the m columns of $\mathbb{I}_\mathcal{C}$ are the standard orthonormal basis vectors $e^\beta \in \mathbb{R}^{nv+1}$ where $\beta \in \mathcal{C}$.

An expression of the second order optimality conditions are facilitated by defining the matrix of constraints $A \in \mathbb{R}^{(m+1)\times(nv+1)}$ from Eq.(29) as

$$A = \begin{bmatrix} (e^*)^T \\ -\mathbb{I}_\mathcal{C}^T \end{bmatrix}. \tag{30}$$

Then, the second order (sufficient) optimality condition on the reduced equality constrained system states that a point satisfying the first order conditions (Eq.29) is a strict local minimum of the problem (Eq.24) if

$$z^T[\Phi]z > 0 \quad \forall\, z \in \text{Null}(A), \tag{31}$$

with $\text{Null}(A)$ denoting the nullspace in the sense $\text{Null}(A) = \{v | Av = 0\ ,\ v \neq 0\}$ (for further details regarding optimality conditions, see Polak (1997, §10.1-10.9) or Luenberger (1989, §2.2)). Thus, although it was mentioned earlier that Φ is in general only semidefinite, it is in fact sufficient for it to be positive definite on the tangent plane defined by the constraints. As a matter of notation the optimal volume fractions will hereafter be denoted by the function

$$\xi^*(\varepsilon, \theta) = \arg\left(\inf_{\xi}\left\{\hat{\Psi}(\varepsilon, \theta, \xi)\right\}\right) \tag{32}$$

Together, Eq.'s(29) and (31) provide the theoretical conditions under which a solution exists for the relaxed free energy with active constraints $\mathcal{C}$. The numerical counterpart to this problem is discussed in Section 4 where the algorithm for determining the active set is outlined. At that time, the properties of the system of equations will be discussed with regard to a physically realistic set of material parameters.

2.3. Thermodynamic Properties

In this section the consequences of the choice of free energy and evolution law are briefly examined. To begin, the stress strain relation is derived from the free energy in the usual manner, the result being

$$\sigma = \xi \cdot \frac{\partial \psi}{\partial \varepsilon} = \sum_{\alpha \in \mathcal{S}} \xi^{\alpha} \mathbb{C} : (\varepsilon - \varepsilon^{\alpha_t} - \Delta\theta \varepsilon^{\alpha_\theta}) \tag{33}$$

where the stress has a contribution from each variant in accordance with its volume fraction. Since the relaxation process starting from a microstructural energy is essentially a homogenization, the stress strain equation is identical to that of a classical Helmholtz mixture of solids. This connection is further strengthened by the fact that the mixture energy bound $\Psi^{\mathrm{M}}_{\mathrm{Reuß}}$ can be derived starting from a classical mixture.

The second law of thermodynamics in the form of the Clausius-Duhem inequality states that the dissipation must be nonnegative. This implies

$$\mathcal{D} = -\frac{\partial \Psi}{\partial \xi} \cdot \dot{\xi} \geq 0. \tag{34}$$

By the first order optimality condition under which the volume fractions evolve, it is clear that this model is dissipation free: $\mathcal{D} = 0$ and hence trivially satisfies the second law. In the following section the implications of the transformation law are examined in detail.

3. TRANSFORMATION SURFACE

The phase transition and reorientation observed to occur in shape memory alloys was originally thought of in terms of phase diagrams, particularly with regard to one dimensional applications (Brinson & Bekker 1997, Govindjee & Kasper 1999). More recently, however, this approach has lost favor as it proved difficult to extend the viewpoint to problems of three dimensions and arbitrary symmetry. However, the fundamental idea of a phase diagram is still a useful one, and in this section it is shown that the bounded partially relaxed free energy function can be used to recover estimates of the austenitic phase diagrams of shape memory materials of arbitrary symmetry.

The viewpoint taken is based on the concept of stability with regard to the crystallographic arrangement. Recalling that the governing energy of the problem is non-convex due to the ability of the material to adjust its microstructure, it is clear that there exists regions in strain and temperature space over which stable arrangements will change. In the general case, which has been eloquently discussed in the context of fluids ((Gurtin 1984, Gurtin, Carr & Slemrod 1984)), there is a marked lack of uniqueness in solutions which minimize the energy. In the above references it was demonstrated that there are at least two ways to overcome this problem: (1) allow the free energy at a constant temperature to also depend upon the strain gradients (hence penalizing rapidly oscillating solutions), or (2) include an energy term which accounts for the existence of interfaces between differing microstructures. Taking an engineering perspective, the first of these would not only be overly difficult to implement, but would require experimental data beyond that which is readily available. However, the second approach is accomplished by the relaxation of the free energy at fixed volume fractions; i.e. the mixture energy $\Psi^{\mathrm{M}}_{\mathrm{Reuß}}$ provides a solution to the stability problem.

Given that our model determines the microstructure volume averages, it is of interest to determine over which domains in strain and temperature space the microstructure is actively "evolving". To specify these regions of transformation, it is helpful to consider a phase change under constant temperature, e.g. a stress induced phase change of the pseudoelastic type. In this case the "spinodal" region ($\mathcal{Y}$) is described by

$$\mathcal{Y} = \{\varepsilon \mid \epsilon : \tfrac{\partial^2 W}{\partial \varepsilon \partial \varepsilon}(\varepsilon, \theta) : \epsilon \leq 0 \quad \forall \epsilon \in \{\mathbb{S}^3 \setminus \mathbf{0}\}\} \tag{35}$$

assuming isothermal conditions. Under this definition, the single crystal energy of Eq.(1), $W = \min_\alpha\{W^\alpha\}$ would appear to have the possible domain of spinodal regions restricted to the sharp intersections of the individual free energies. However, through the optimization procedure these sharp interfaces are "unfolded" into spaces of one higher order. The end result is that the phase diagram may be reformulated in terms of the volume fractions which appear in the partially relaxed free energy. For example, the region of the phase diagram which contains austenite in the microstructure is given by the set $\mathcal{P}_a \in \mathbb{S}^3 \times \mathbb{R}_+$ defined as

$$\mathcal{P}_a = \{(\epsilon, \theta) \mid 0 \leq \xi^{a^*}(\epsilon, \theta) \leq 1 \ , \ \epsilon \in \mathbb{S}^3 \ , \ \theta \in \mathbb{R}_+\} \tag{36}$$

with $\boldsymbol{\xi}^*$ defined from Eq.(32). In the literature on shape memory alloys the transformation surfaces (or "yield" surfaces (Huang 1999)) are defined by the limits $\xi^{a^*}(\epsilon, \theta) = 1$ and $\xi^{a^*}(\epsilon, \theta) = 0$. Typically these are given in stress-temperature space; here we select a strain space representation as it is more natural in this setting.

Two examples which demonstrate the above ideas for a specific material are given below. The case studies concern phase diagrams near the dilational axis and in plane strain space respectively. Since the numerical methods needed to determine the phase diagram are shared by the discrete implementation presented in Section 4, the details are deferred until then.

The material properties in both examples approximate that of a Cu-Al-Ni alloy which undergoes a cubic $\leftrightarrow$ orthorhombic change in the symmetry of its crystallographic lattice. The six lattice correspondents of the material are identified by number; austenite is denoted by a. The material parameters and references to the original experiments are provided in Appendix A, whereas the free energy is as previously given.

3.1. Dilation Axis

Due to the availability of an expression for the partially relaxed free energy, the computation of the transformation surfaces can be performed in a straightforward manner. As a first example the phase diagram near the dilational axis is examined. By setting the shear strains to zero, and allowing ε_{11}, ε_{22}, and ε_{33} to vary, the transformation surfaces surrounding the dilational axis can be plotted. This case is of interest since it is well known that a purely dilational strain state hinders the phase change in shape memory alloys.

The surfaces which appear in Figures 1 through 5 coincide with the set of points

$$\mathcal{P}_\alpha^\nu = \{\epsilon \mid \xi^{\alpha^*}(\epsilon, \theta) = \nu \ , \ \epsilon \in \mathbb{S}^3 \ , \ \theta \in \mathbb{R}_+\}. \tag{37}$$

This gives the boundary of the region as defined in Eq.(36) when $\alpha = a$ and $\nu = 0$ or 1. For example, Figure 1 shows all of the phase variant surfaces plotted for $\nu = 0$ and $\theta = \theta_o$. In the

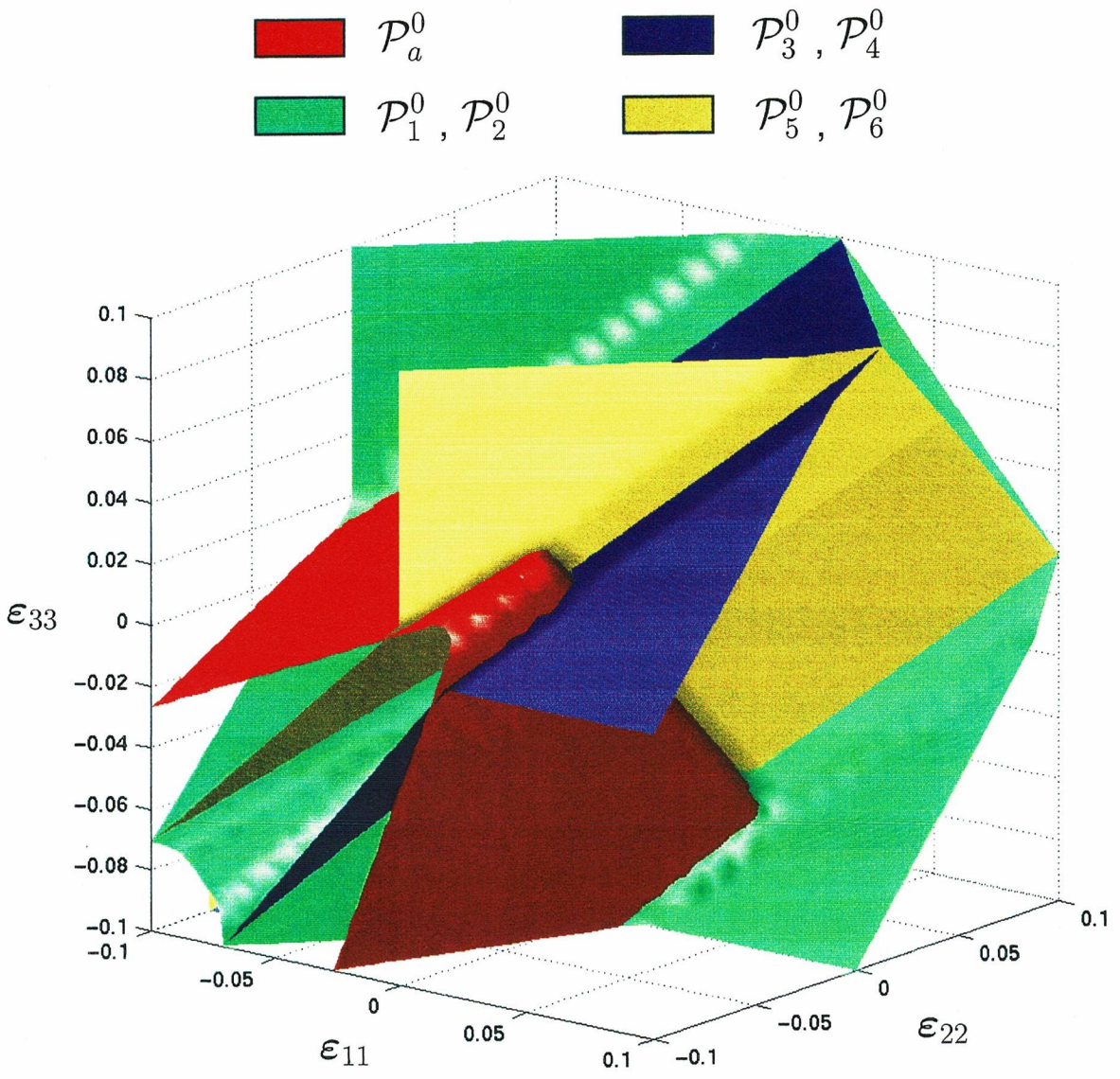

Figure 1. Section cut of the phase diagram for a Cu-Al-Ni shape memory alloy near the dilational axis. The strain components not shown are set to zero, and the temperature is fixed at $\theta = \theta_o$. The notation for the surfaces is defined in Eq.(37).

plot only the austenite zero fraction surface and three martensitic zero fraction surfaces appear. The first and second, third and fourth, and fifth and sixth martensitic surfaces are respectively identical due to the symmetry of their Bain strains with respect to this region of stress-temperature space. Here, the volume fraction of austenite is zero for all points exterior to the right (along the dilational tension line) of the red ($\mathcal{P}_a^0$) boundary. Likewise, all points away from the viewer on surfaces ($\mathcal{P}_1^0, \mathcal{P}_2^0$), all points to the upper left of surfaces ($\mathcal{P}_3^0, \mathcal{P}_4^0$), and all points toward the viewer for surfaces ($\mathcal{P}_5^0, \mathcal{P}_6^0$) have zero as the volume fraction corresponding to the surface number. To

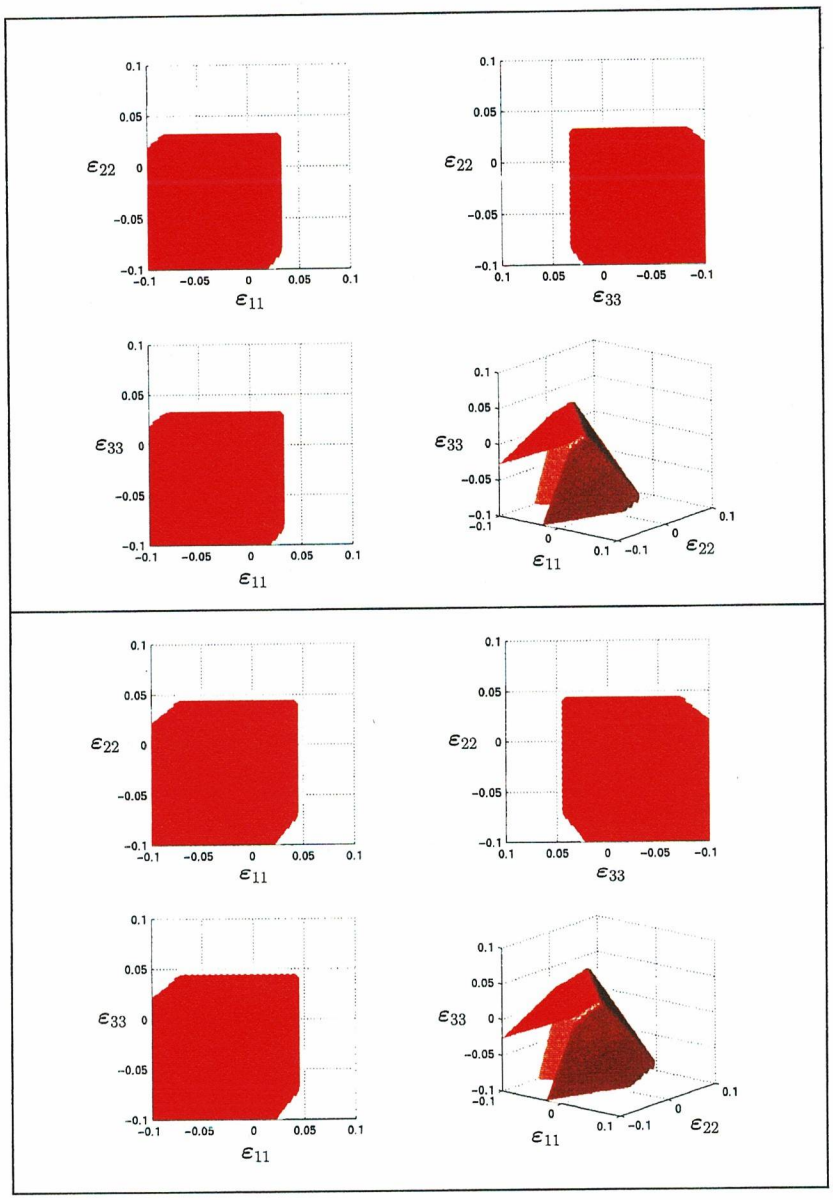

Figure 2. Views of the boundary $\mathcal{P}_a^0 \subset \mathcal{P}_a$ near the dilational axis. The temperatures at which the the top and bottom halves of the figure were computed are $\Delta\theta = -20$ and $\Delta\theta = 20$, respectively.

give an example, the point $\varepsilon_{11} = \varepsilon_{22} = -0.1$, $\varepsilon_{33} = 0.1$ has a microstructure whose zero volume fractions are $\xi^a = \xi^3 = \xi^4 = 0$. From this plot it can be seen that the bounding surface beyond which austenite (in red) is zero is symmetric about the dilational axis and grows in proportion to the compression.

A clearer picture of this is obtained by plotting just the austenite $\nu = 0$ surface as is done in Figure 2. The upper half of this figure provides top, front, right side, and isometric views of the austenite surface at a temperature of $\theta - \theta_o = -20$, and is repeated in the lower half of the figure

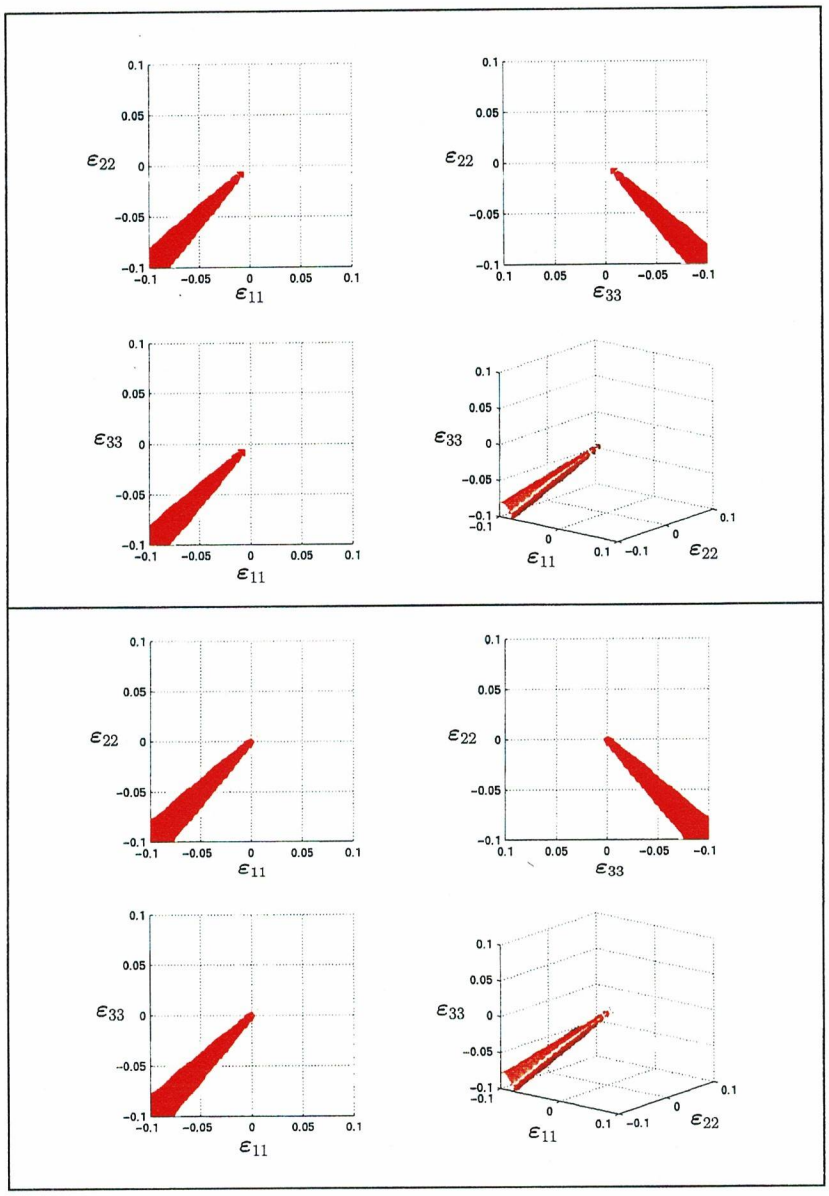

Figure 3. Views of the boundary $\mathcal{P}_a^1 \subset \mathcal{P}_a$ near the dilational axis; $\Delta\theta = -20$ in the top half of the figure and $\Delta\theta = 20$ in the bottom half.

for $\theta - \theta_o = 20$. By contrasting the top and bottom of the figure, it can be seen that temperature has the effect of scaling and translating the transition surface, but does not effect its shape over this temperature range. It is also interesting that there is a nearly flat surface with the dilational tension axis as its normal beyond which (in the direction of its normal) austenite cannot be induced.

Figure 3 shows the austenite bounding surface $\mathcal{P}_a^1$ at the temperatures $\theta - \theta_o = -20$ and $\theta - \theta_o = 20$ as was done in Figure 2. By comparing Figures 3 and 2 it is clear that for this region of the phase diagram pure austenite occupies the cone oriented along the compression axis. By

comparing the upper and lower half of Figure 3, it is seen that temperature variations (in the range plotted) only serve to translate the cutoff point above which dilational compression completely inhibits phase change from occurring.

3.2. Plane Strain

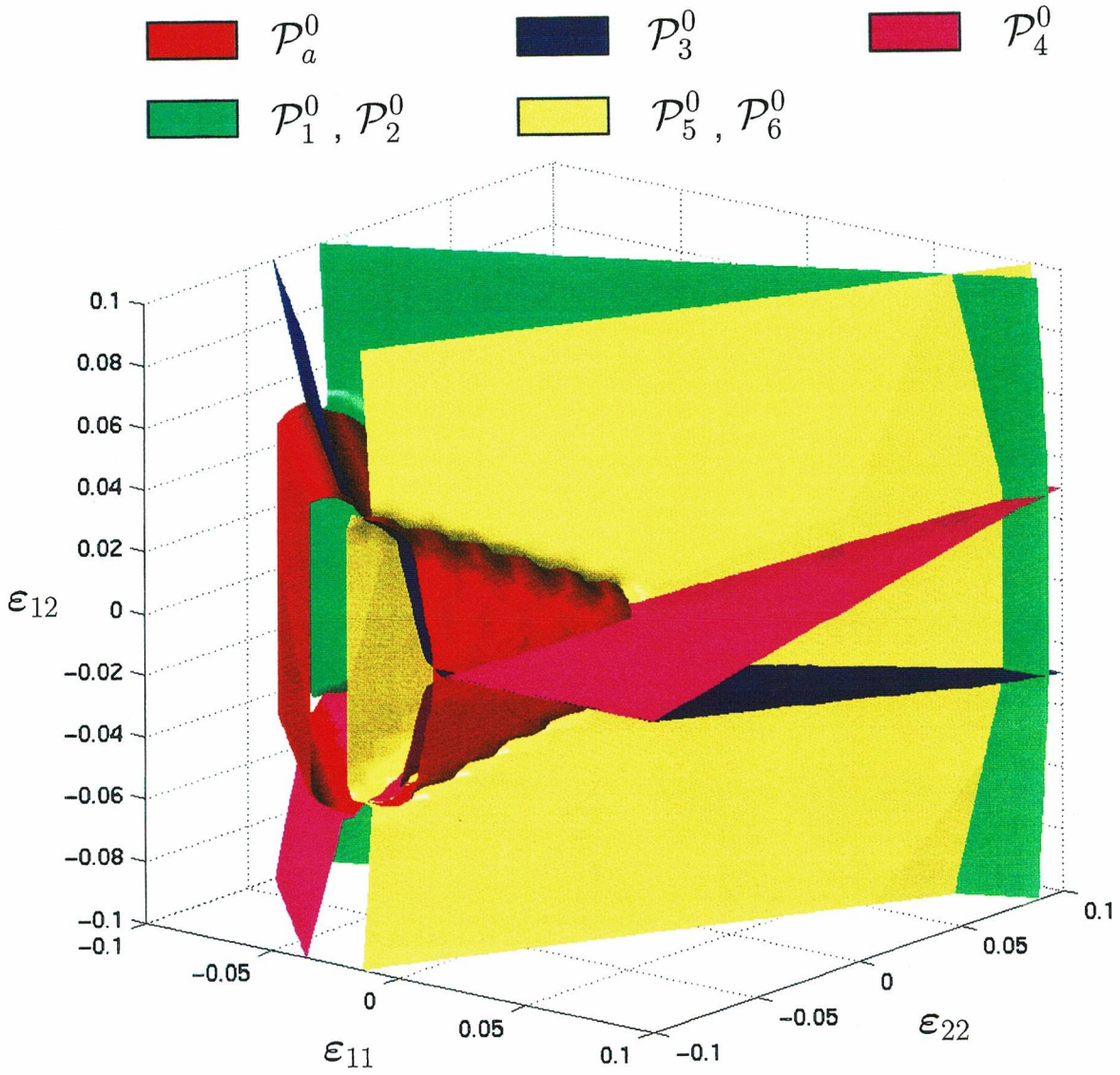

Figure 4. Projection of phase diagram onto plane strain region at the reference temperature. The surfaces demarcate boundaries of zero volume fraction.

The next series of phase diagram projections were computed under the conditions of plane strain, $\varepsilon_{33} = \varepsilon_{13} = \varepsilon_{23} = 0$. From the perspective of phase transition from a cubic crystal lattice, plane strain is less restrictive than hydrostatic conditions; this is reflected in the plots. The first, Figure 4,

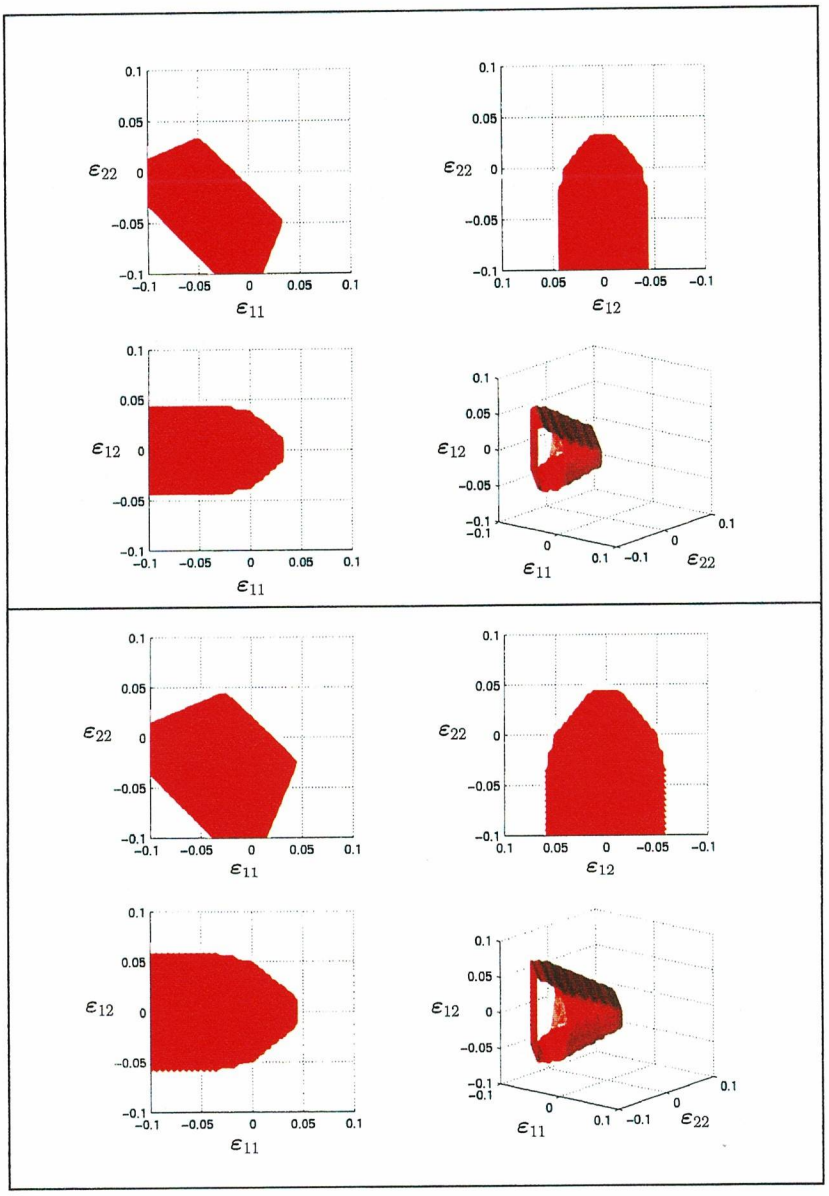

Figure 5. A portion of the surface $\mathcal{P}_a^0$ in plane strain space at $\Delta\theta = -20$ (top) and $\Delta\theta = 20$ (bottom). Note the symmetry about the shear axis.

shows five surfaces $\mathcal{P}_\alpha^0$ crossing a given region of strain space at $\theta = \theta_o$. The austenite surface, in red, is prominent on the left side of the plot; beyond this is a region comprised of twinned martensites. The volume fraction of austenite is zero for all points exterior to the enclosed volume. Similarly this is true for all points away from the viewer behind surface $\mathcal{P}_1^0, \mathcal{P}_2^0$, all points below surface $\mathcal{P}_3^0$, all points above surface $\mathcal{P}_4^0$, and all points toward the viewer for surface $\mathcal{P}_5^0, \mathcal{P}_6^0$. As an example, the point $\varepsilon_{11} = \varepsilon_{22} = -0.1$, $\varepsilon_{12} = 0$, and $\theta = \theta_o$ has a microstructure whose volume fractions are $\xi^1 = \xi^2 = \xi^5 = \xi^6 = \frac{1}{4}$. Note that the boundaries of lattice correspondent variants $(\mathcal{P}_1^0, \mathcal{P}_2^0)$ and $(\mathcal{P}_5^0, \mathcal{P}_6^0)$ are identical in this region of strain space.

Another view of the austenite boundary is provided in Figure 5, where again the upper part is 20 degrees above the reference temperature, and the lower half is 20 degrees below the reference temperature. As was noted earlier, temperature changes serve to shift the centroid and scale the surface geometry of the phase boundaries in strain space. Beyond this, it is interesting that all of the plots indicate a lack of symmetry with respect to tension and compression states. This coincides well with experimental evidence of tension-compression asymmetry in shape memory alloys (Gall & Sehitoglu 1999, Gall, Sehitoglu, Chumlyakov & Kireeva 1999).

4. CONSTITUTIVE EVALUATION STRATEGY

The purpose of this section is to summarize the numerical techniques necessary to determine the evolution of microstructure for arbitrary boundary value problems in a manner consistent with the constitutive equations of Section 2. It will be assumed that the model is to be incorporated in a typical finite element code which provides to the constitutive subroutine at each Gauss point a strain $\boldsymbol{\varepsilon}_{n+1}$ and temperature θ_{n+1} coinciding with time t_{n+1}. Thus, there are three steps to be considered; the discrete time integration of the continuum equations; determining a means for solving the constitutive equations; and specification of the algorithmic tangent. Note that the second step also provides the means to compute the phase boundary surfaces of Section 3.

Since the model has no history variables or rate dependence, the time integration is a picayune matter. It will simply be implied that all quantities are taken to exist at time t_{n+1}, and the subscripts will be dropped. However, it is worth mentioning that the first step performed by the constitution is to compute $\boldsymbol{\psi}$, $\boldsymbol{\phi}$, and $\boldsymbol{\Phi}$ consistent with Eq.'s (8), (15), and (16) respectively as they are constants during the ensuing optimization.

A consistent solution of the constitutive equations requires the evaluation of $\boldsymbol{\xi}^*(\boldsymbol{\varepsilon}, \theta)$ as defined by Eq.(32). This is pursued through the use of an active set strategy (Luenberger 1989), an outline of which is as follows. First the volume fractions $\boldsymbol{\xi}$ and an active set $\mathcal{C} \subset \mathcal{S}$ are specified, a logical choice being the solution from the previous time step should it be available. The next step is to solve the equality constrained problem consistent with $\mathcal{C}$. The solution is the trial set $\boldsymbol{\xi}^*_{trial}$, $\boldsymbol{\gamma}_{trial}$, and δ_{trial}. At this point the set of inactive constraints $\mathcal{I} = \{\mathcal{S} \setminus \mathcal{C}\}$ should be checked with the worst offender being added to the set of constraints and the system subsequently resolved. Likewise, constraints can be removed from the active set when the corresponding lagrange multiplier in $\boldsymbol{\gamma}$ is negative, again requiring the updated system to be resolved. When a trial set is found which does not violate the constraints and has only nonnegative lagrange multipliers, $\boldsymbol{\xi}^*$ is set to the trial value and the optimization step is complete.

During the course of the active set iteration just described, it is necessary to repeatedly solve the first order optimality conditions with various sets of constraints. However, as it is currently written,

$$\begin{Bmatrix} \frac{1}{2}\boldsymbol{\phi} - \boldsymbol{\psi} \\ 1 \\ \mathbf{0} \end{Bmatrix} = \begin{bmatrix} \boldsymbol{\Phi} & \boldsymbol{e}^* & -\mathbb{I}_{\mathcal{C}} \\ (\boldsymbol{e}^*)^T & 0 & 0 \\ -\mathbb{I}_{\mathcal{C}}^T & 0 & 0 \end{bmatrix} \begin{Bmatrix} \boldsymbol{\xi} \\ \delta \\ \bar{\boldsymbol{\gamma}} \end{Bmatrix} = \begin{bmatrix} \boldsymbol{\Phi} & A^T \\ A & \mathbf{0} \end{bmatrix} \begin{Bmatrix} \boldsymbol{\xi} \\ \delta \\ \bar{\boldsymbol{\gamma}} \end{Bmatrix} \tag{38}$$

the system is poorly conditioned due the order of the terms in $\boldsymbol{\Phi}$ compared with those in A. As a

way to avoid a loss in accuracy, the equation set is replaced by

$$\left\{ \begin{array}{c} \frac{1}{2}\phi - \psi \\ \eta \\ 0 \end{array} \right\} = \left[\begin{array}{cc} \Phi & \eta A^T \\ \eta A & 0 \end{array} \right] \left\{ \begin{array}{c} \xi \\ \tilde{\delta} \\ \tilde{\gamma} \end{array} \right\} \tag{39}$$

where η is of the order of the norm of Φ, and $\tilde{\delta}$, $\tilde{\gamma}$ are related to δ , γ via η. By scaling in this manner, the only effect is an improvement in the numerical properties of the system. Note that it is a simple matter to verify the second order optimality condition during the solution stage.

With the volume fractions $\boldsymbol{\xi}^*$ in hand, the stress is computed according to Eq.(33). Then, since temperature is taken as an assigned field, the only remaining issue is to specify the consistent tangent operator, i.e. the linearization of the constitutive equations which determine the stress from the input strain (Simo & Taylor 1986). To that end the variation of the stress is

$$\delta\boldsymbol{\sigma} = \sum_{\alpha \in S} \delta\xi^{\alpha^*} \frac{\partial \psi^\alpha}{\partial \boldsymbol{\varepsilon}} + \xi^{\alpha^*} \frac{\partial^2 \psi^\alpha}{\partial \boldsymbol{\varepsilon} \partial \boldsymbol{\varepsilon}} : \delta\boldsymbol{\varepsilon} \tag{40}$$

where the first term on the right hand side is equivalent to $\delta\xi^{\alpha^*} = (\partial_{\boldsymbol{\varepsilon}} \xi^{\alpha^*}) : \delta\boldsymbol{\varepsilon}$. To get at an expression for $\partial_{\boldsymbol{\varepsilon}} \xi^{\alpha^*}$, it is convenient to write out the final solution of the active set iteration symbolically. Doing so gives

$$\left\{ \begin{array}{c} \boldsymbol{\xi}^* \\ \tilde{\delta}^* \\ \tilde{\gamma}^* \end{array} \right\} = \left[\begin{array}{cc} \Xi & V^T \\ V & H \end{array} \right] \left\{ \begin{array}{c} \frac{1}{2}\phi - \psi \\ \eta \\ 0 \end{array} \right\} = \left\{ \begin{array}{c} \Xi\{\frac{1}{2}\phi - \psi\} + V^T \left\{ \begin{array}{c} \eta \\ 0 \end{array} \right\} \\ V\{\frac{1}{2}\phi - \psi\} + H \left\{ \begin{array}{c} \eta \\ 0 \end{array} \right\} \end{array} \right\}. \tag{41}$$

Since the only terms in the last column on the right that vary with strain are ψ, Eq.(40) can be expressed as

$$\delta\boldsymbol{\sigma} = \left\{ \sum_{\alpha \in S} \xi^{\alpha^*} \frac{\partial^2 \psi^\alpha}{\partial \boldsymbol{\varepsilon} \partial \boldsymbol{\varepsilon}} - \sum_{\alpha \in S} \sum_{\beta \in S} \Xi^{\alpha\beta} \frac{\partial \psi^\alpha}{\partial \boldsymbol{\varepsilon}} \otimes \frac{\partial \psi^\beta}{\partial \boldsymbol{\varepsilon}} \right\} : \delta\boldsymbol{\varepsilon} \tag{42}$$

where the term in brackets is the algorithmic tangent. Note that the tangent is symmetric and requires only the upper left $nv + 1$ block of the final active set iteration solution (Ξ) which does not carry the scaling factor η. To conclude this section we summarize the constitutive equations in Table 1.

5. NUMERICAL EXAMPLES

In this section three experimental tests conducted by Shield (1995) are simulated using the model outlined up to this point. The intent is to demonstrate that detailed information regarding the spatial variation of microstructure on the global scale can be obtained from the model. Further it is shown that the mechanical response, though dissipation free, provides realistic estimates of the transformation stresses observed in the experiment. Finally, it is demonstrated that the model has favorable global convergence properties.

The experimental tests upon which the simulations are based have the designations A1-T1b, A1-T2b, and A1-T3b in the paper by Shield. Each is a tensile test under fixed end conditions with three

Table 1. Constitutive Equation Summary.

1. Volume fractions:

$$\boldsymbol{\xi}^*(\boldsymbol{\varepsilon},\theta) = \arg\left(\inf_{\boldsymbol{\xi}}\left\{\hat{\Psi}(\boldsymbol{\varepsilon},\theta,\boldsymbol{\xi})\right\}\right) \tag{43}$$

2. Stress-strain:

$$\boldsymbol{\sigma}^\alpha = \mathbb{C}:(\boldsymbol{\varepsilon} - \boldsymbol{\varepsilon}^{\alpha_t} - \Delta\theta\boldsymbol{\varepsilon}^{\alpha_\theta}) \tag{44}$$

$$\boldsymbol{\sigma} = \sum_{\alpha\in\mathcal{S}} \xi^{\alpha^*}\boldsymbol{\sigma}^\alpha \tag{45}$$

3. Consistent tangent:

$$\mathbb{C}^{\text{alg}} = \mathbb{C} - \sum_{\alpha\in\mathcal{S}}\sum_{\beta\in\mathcal{S}} \Xi^{\alpha\beta}\boldsymbol{\sigma}^\alpha \otimes \boldsymbol{\sigma}^\beta \tag{46}$$

different crystallographic orientations for the tensile axis of a Cu-Al-Ni single crystal. The details of the material properties and the orientations of the tests are discussed in Appendix A. The finite element mesh used in the numerical tests consisted of a grid of 19 by 6 by 1 standard displacement eight node bricks covering the 38mm by 6mm by 1mm geometry of the idealized specimen. The boundary conditions consisted of fixed degrees of freedom at each end of the bar which were used to drive the displacement along the primary axis under isothermal conditions. Although the maximum axial strain in the experiments never exceeded 0.03, each of the simulations were run out to 0.06 in an effort to test the constitution over a wider range. The first results reported regard the microstructure evolution at a point close to the center of the mesh.

5.1. Volume Fraction History

The results presented in this section summarize the volume fraction evolution as simulated near the center of the bar for the three test configurations. The initial microstructure conditions of each run were set to pure austenite in accordance with the observed pseudoelastic behavior in the experiments; the temperature was fixed both spatially and temporally to 313 Kelvin in the simulations. Note that although the dogbone geometry of the experimental samples differs from the straight bar used in the simulation, the results should not be affected significantly near the center of the bar.

Figures 6, 7, and 8 present the simulated response from experiments A1-T1b, A1-T2b, and A1-T3b respectively. In each case the volume fractions can be read along the vertical axis, while the horizontal axis provides the load factor as computed from the current displacement of the bar divided by the maximum displacement in the simulation. Of interest is the predicted formation of lattice correspondent twins as inferred from the volume fractions arising out of the relaxed theory. In the experiments, the twins reported were estimated based on the angles of the microstructure patterns observed at the surface of the specimens and the use of crystallographic theory to determine which variants might be consistent with those observations.

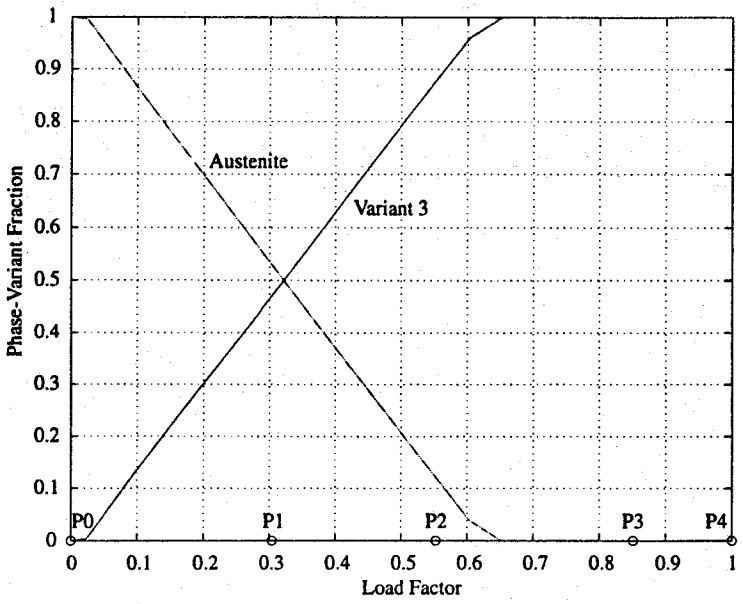

Figure 6. Evolution of volume fractions vs. load factor for simulation of experiment A1-T1b. The lattice correspondent variants inferred from the experiment were $(1, 2, 3)$ in contrast to just variant 3 in the simulation.

Comparing the variant formation inferred from the experiment and the simulation (Figure 8) of run A1-T3b, it is found that in both cases lattice correspondents 2, 3, and 6 (as ordered in Appendix A) formed during the phase transition from austenite. Similarly, the inferred lattice correspondents 2 and 6 from the experiment and the simulation (Figure 7) of run A1-T2b match exactly. Only for run A1-T1b (Figure 8) was there a discrepancy between the variants inferred from the experiment and the simulation. Here, the experiment suggested variants 1, 2, and 3 whereas the simulation predicted a transformation from austenite to just lattice correspondent variant 3. Given that austenite is rank one incompatible with the martensitic variants, this incongruity may be at least in part due to the fact that the mixture function is an approximation, as are the isotropic/isomodular assumptions.

Note that along the bottom of each of the figures there are a series of five points indicated by the hollow circles and labeled P0 through P4. These locate with respect to the load the plots of the spatial variation of the volume fractions as given in the next section.

5.2. Spatial Variation of the Microstructure

The volume fraction histories of the previous section outline the system evolution at a single point near the center of the mesh for the entire load history. In this section the spatial variation of the volume fractions over the entire mesh is given at specific points on the load curve. The chosen points are indicated in Figures 6 through 8 by the circled points; for each run they are labeled as points P0 through P4 (see Figure 12 to locate the points on the mechanical response curve). The results are organized by run as A1-T1b, A1-T2b, and A1-T3b in Figures 9, 10, and 11. Within each figure the five boxed regions coincide with P0 through P4 as previously mentioned. Further, within each box there are four plots showing the spatial variation of the variants which are labeled

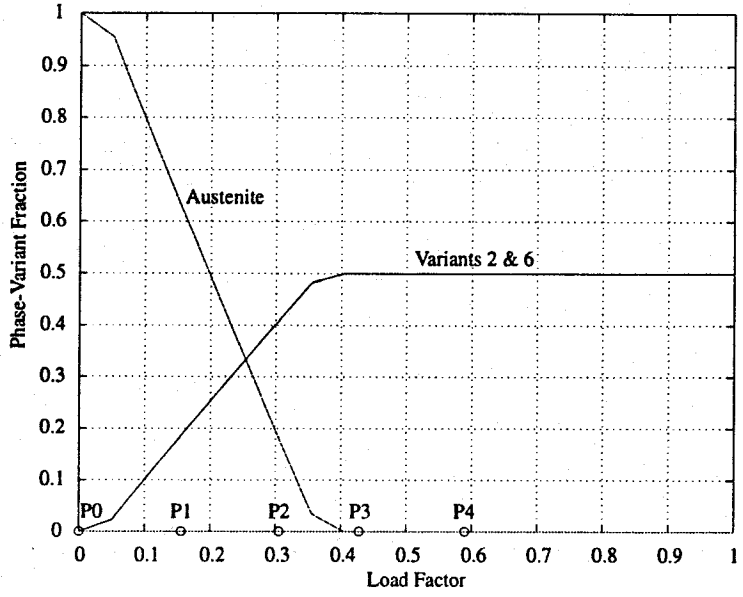

Figure 7. Evolution of volume fractions vs. load factor for simulation of experiment A1-T2b. The lattice correspondent variants inferred from the experiment were $(2, 6)$ which matches those predicted by the simulation.

consistent with the lattice correspondent numbering. Finally, the large centered mesh in each box is the deformed mesh shown to scale. Note that although the mesh is three dimensional, the plots only show the profile in the following figures.

One of the essential features which is displayed by each run is a strong sensitivity to the boundary conditions at the end of the bar. In each case the added constraints of the fixed boundary condition near the attachment to the testing machine hinders the phase transformation from austenite to martensite. This is evidenced in the figures by the regions which develop near the simulated grips and generally transform much later in the load curve than the relatively unrestrained region in the middle of the bar. The effect is entirely consistent with the phase diagrams of Section 3, and in particular the shape of the transformation surface in Figures 1 and 2 where it can be seen that the points near the restrained grips would naturally be expected to transform at higher strain levels.

The individual runs also show unique characteristics which distinguish them from one another. For example, while A1-T1b (Figure 9) has a highly symmetric transformation profile with respect to the major axes of the specimen, runs A1-T3b (Fig. 11) and A1-T2b (Fig. 10) have a more diagonal band pattern. The differences are the manifestation of the orientation dependence of the single crystal response despite the fact elastic anisotropy has not been included.

Also of note is the shape of the deformed mesh for A1-T2b as seen by careful examination of the final plot in Figure 10. Here, the transformation strains appear to have a significant shear component along the horizontal axis in the plane of the Figure. However, since the ends are restrained from translation, the Bain strain is realized in the sinusoidal deformed shape (consistent with the boundary conditions) visible in the final plot. It is open to speculation as to whether or not this major axis bending predicted by the simulation may have been a factor in the experiment and the failure of the specimen during the transformation.

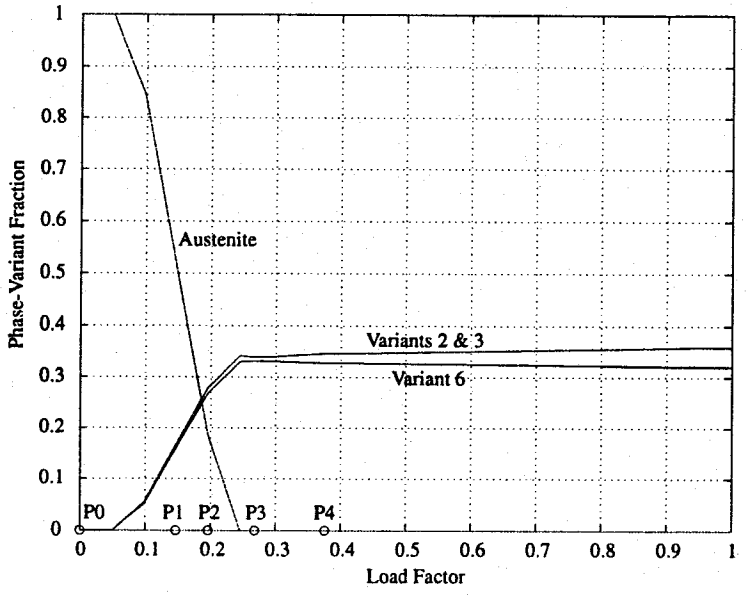

Figure 8. Evolution of volume fractions vs. load factor for simulation of experiment A1-T3b. The lattice correspondent variants inferred from the experiment were $(2, 3, 6)$ which matches those predicted by the simulation.

Before presenting the mechanical response curves of the simulations, it is worth mentioning that due to the use of a relaxed free energy function the results of this section do not exhibit mesh dependence or lack of uniqueness as would be expected from the non-convex microstructural energy function.

5.3. Mechanical Response

Figure 12 shows the simulated mechanical response for the three runs A1-T1b, A1-T2b, and A1-T3b in the form of a stress strain plot, where infinitesimal theory was used to generate the curves from the global response of the simulated bar. Although the relaxed model does not include hysteresis, the quantitative predictions regarding transformation stress, change in response with respect to orientation, and the range of transformation strains match remarkably well with the experiments, particularly given the simplicity of the analysis.

To correlate the mechanical response with previous results regarding the variation of volume fractions both spatially and at various points in the simulation, each curve has the five points P0 through P4 labeled. These points are again referred to in the next section where the convergence properties of the model are discussed.

5.4. Convergence Properties

All of the computations presented were carried out using standard symmetric Newton-Raphson solution strategies for the global iteration. The only non-standard technique employed was to adjust the time step (load increment) using feedback from the constitution in the following manner. Having solved for the updated volume fractions, stress, and consistent tangent, each Gauss point would

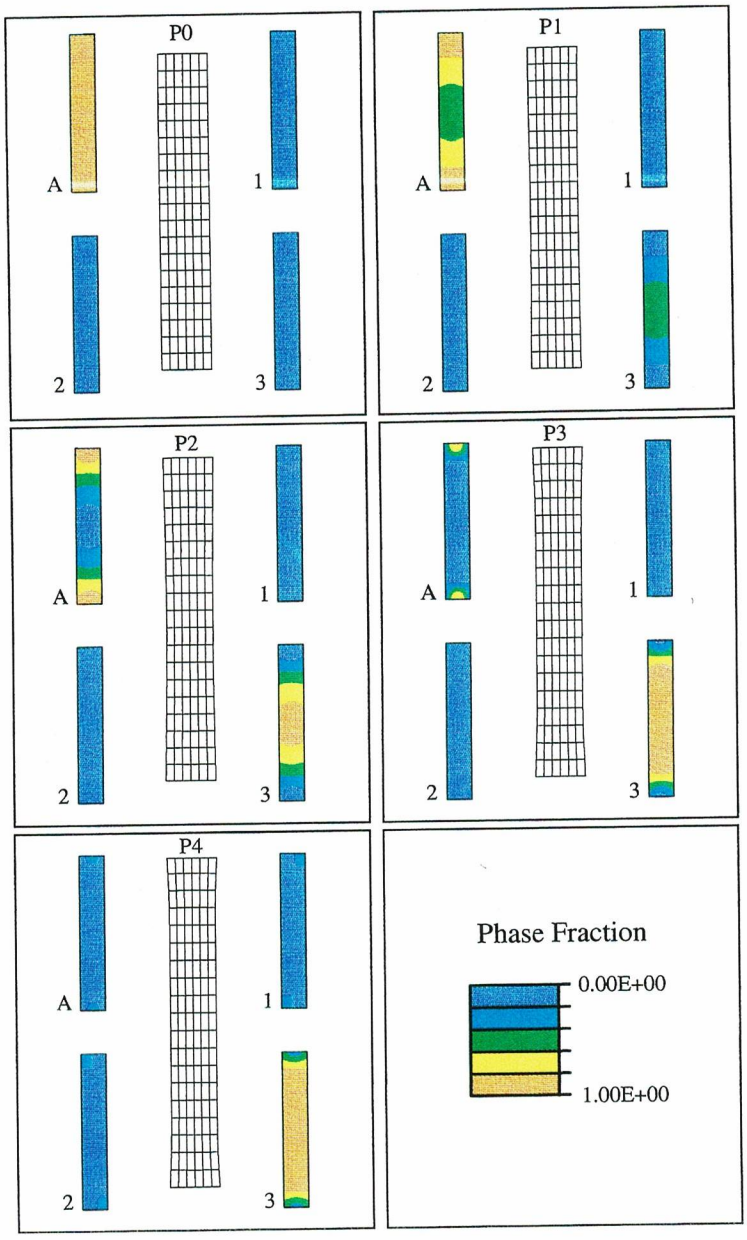

Figure 9. Spatial variation of microstructure for the simulation of experiment A1-T1b. The plots ordered left to right and top to bottom are snapshots at the times indicated by P0 through P4 throughout this section. Within each subfigure the four outer plots show the spatial variation of the indicated variant, while the center mesh shows the deformation to scale.

additionally compute the value $r_m = \|\boldsymbol{\xi}_{n+1} - \boldsymbol{\xi}_n\|_\infty / \zeta$ and return the value to the global solution routine. The solver could then be programmed to decrease or increase the timestep according to variations in r_m. For example, by specifying a value of ζ one could assure that the maximum change in volume fractions at any given point in the mesh would not exceed ζ in one time step. This is particularly useful to avoid missing the transitional regions in material behavior such as the initial

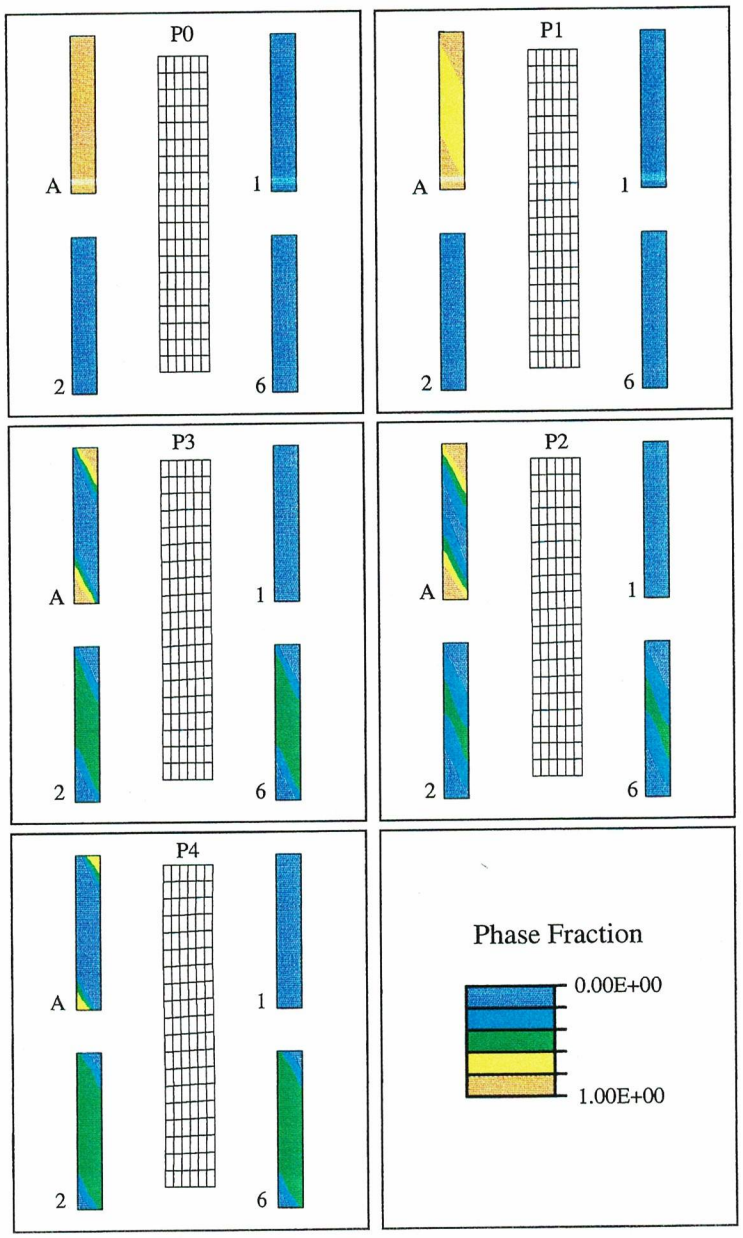

Figure 10. Spatial variation of microstructure for the simulation of experiment A1-T2b. The plots ordered left to right and top to bottom are snapshots at the times indicated by P0 through P4 throughout this section. Within each subfigure the four outer plots show the spatial variation of the indicated variant, while the center mesh shows the deformation to scale.

stages of a phase change as was done here.

Table 2 shows the convergence behavior of the global iteration for points near the beginning, middle, and end of the transformation in terms of the residual norm and the normalized residual norm. As evidenced by these typical results, the model has good global convergence properties.

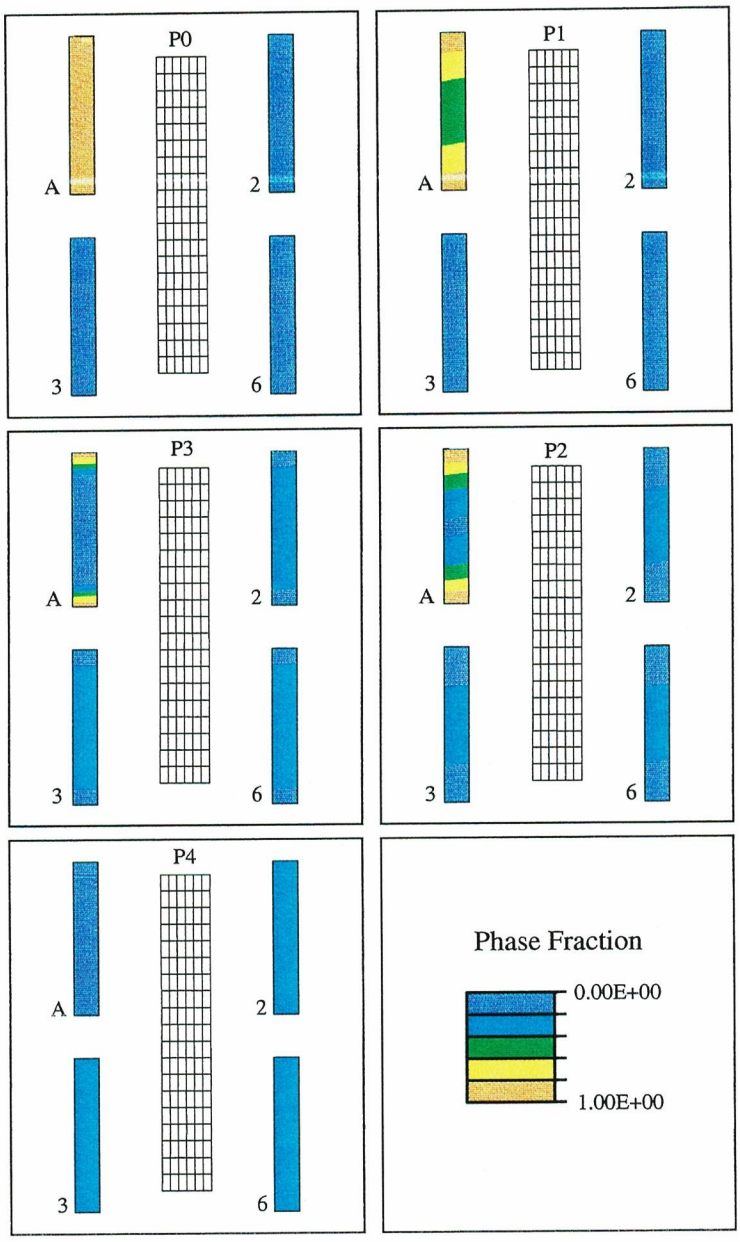

Figure 11. Spatial variation of microstructure for the simulation of experiment A1-T3b. The plots ordered left to right and top to bottom are snapshots at the times indicated by P0 through P4 throughout this section. Within each subfigure the four outer plots show the spatial variation of the indicated variant, while the center mesh shows the deformation to scale.

6. DISCUSSION

The purpose of this paper was to develop and demonstrate applications of an approximate partially relaxed free energy function for the analysis of shape memory alloys. To that end a simple method for estimating the austenitic phase diagram was developed which links the early one dimensional

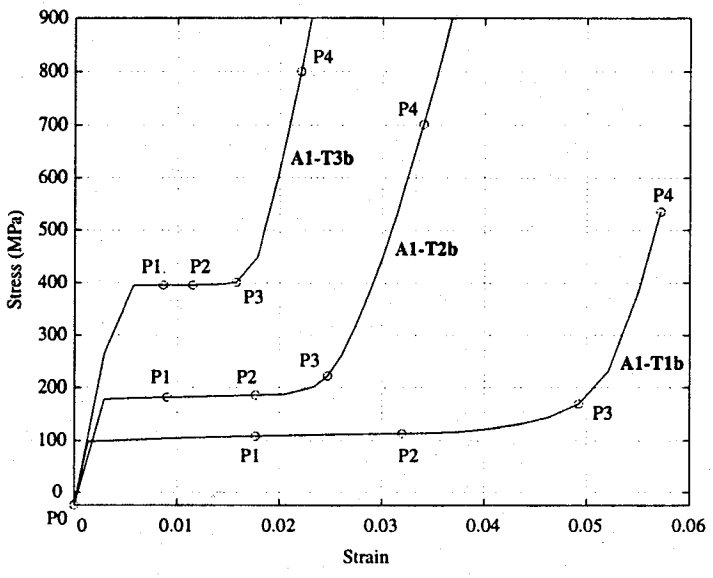

Figure 12. Mechanical response of the three simulated experiments. The labeled points correspond with the microstructures shown in Figures 9 through 11.

empirical phase diagram models to the body of literature viewing the problem strictly from the viewpoint of elastic stability. Further, it was demonstrated that the approach provides a simple implementation suitable for finite element analysis which has desirable numerical properties and, more importantly, makes realistic quantitative predictions regarding the evolution of the lattice correspondent variants, transitional stress and strain levels, and orientation dependence.

ACKNOWLEDGMENTS

The authors gratefully acknowledge the support of the Lawrence Livermore National Laboratory through subcontract B502681 to prime contract W-7405-ENG-48. SG dankt der Alexander von Humboldt-Stiftung für die Verleihung eines Forschungsstipendium an der Universität Stuttgart.

REFERENCES

Abeyaratne, R., S.J. Kim & J.K. Knowles. 1994. "A One-Dimensional Continuum Model for Shape-Memory Alloys." *International Journal of Solids and Structures* 31:2229–2249.

Achenbach, M. & I. Müller. 1985. "Simulation of Material Behavior of Alloys with Shape Memory." *Archives of Mechanics* 35:537–585.

Ball, J.M. & R.D. James. 1987. "Fine Phase Mixtures as Minimizers of Energy." *Archive for Rational Mechanics and Analysis* 100:13–52.

Ball, J.M. & R.D. James. 1992. "Proposed Experimental Tests of a Theory of Fine Microstructure and the Two-Well Problem." *Philosophical Transactions of the Royal Society of London, Series A* 338(1650):389–450.

Bhattacharya, K. 1993. "The Microstructure of Martensite and its Implications for the Shape-Memory Effect." *Microstructure and Phase Transition; The IMA Volumes in Mathematics and its Applications* Springer Verlag, pp. 1–25.

Table 2. Typical global residual norm convergence examples.

Residual Norm	Normalized
Simulation A1-T1b, Point P1	
1.0746074E+04	1.0000000E+00
7.7893395E+00	7.2485447E-04
3.3494279E-11	3.1168853E-15
Simulation A1-T2b, Point P2	
1.3558430E+04	1.0000000E+00
2.3415629E+01	1.7270162E-03
2.9254678E-11	2.1576744E-15
Simulation A1-T3b, Point P4	
8.7710061E+03	1.0000000E+00
7.3920735E+02	8.4278514E-02
2.0549854E+01	2.3429301E-03
2.0952780E-01	2.3888685E-05
2.4765278E-11	2.8235391E-15

Bhattacharya, K. & G. Dolzmann. 2000. "Relaxed Constitutive Equations for Phase Transforming Materials." *Journal of the Mechanics and Physics of Solids* 48:1493–1517.

Bhattacharya, K. & R.V. Kohn. 1996. "Symmetry, Texture, and the Recoverable Strain of Shape Memory Alloys." *Acta Metallurgica* 44:529–542.

Boyd, J.G. & D.C. Lagoudas. 1996. "A Thermodynamic Constitutive Model for the Shape Memory Materials. Part I. The monolithic shape memory alloy." *International Journal of Plasticity* 12:805–842.

Brinson, L.C. & A. Bekker. 1997. "Temperature-Induced Phase Transformation in a Shape Memory Alloy: Phase Diagram Based Kinetics Approach." *Journal of the Mechanics and Physics of Solids* 45:949–988.

Brinson, L.C. & R. Lammering. 1993. "Finite Element Analysis of the Behavior of Shape Memory Alloys and their Applications." *International Journal of Solids and Structures* 30:3261–3280.

Carstensen, C.; Plecháč, P. 1997. "Numerical solution of the scalar double-well problem allowing microstructure." *Mathematics of Computation* 66:997–1026.

Carstensen, C.; Plecháč, P. 2000. "Numerical analysis of compatible phase transitions in elastic solids." *SIAM Journal on Numerical Analysis* 37:2061–2081.

Dacorogna, Bernard. 1989. *Direct methods in the calculus of variations.* Springer Verlag. Also listed under: Applied mathematical sciences (Springer-Verlag New York Inc.); v. 78.

Ericksen, J.L. 1986. "Constitutive Theory for Some Constrained Elastic Crystals." *International Journal of Solids and Structures* 22:951–964.

Ericksen, J.L. 1989. "Weak Martensitic Transformations in Bravais Lattices." *Archive for Rational Mechanics and Analysis* 107:23–36.

Gall, K. & H. Sehitoglu. 1999. "The Role of Texture in Tension-Compression Asymmetry in Polycrystalline NiTi." *International Journal of Plasticity* 15:69–92.

Gall, K., H. Sehitoglu, Y.I. Chumlyakov & I.V. Kireeva. 1999. "Tension-Compression Asymmetry of the Stress Strain Response in Aged Single Crystal and Polycrystalline NiTi." *Acta Materialia* 47:1203–1217.

Govindjee, S. & A. Mielke. 2000. "The free-energy of mixing for evolving martensitic materials by quasi-convex analysis." *in preparation* .

Govindjee, S. & C. Miehe. 2000. "A Multi-Variant Martensitic Phase Transformation Mode: Formulation and Numerical Implementation." *in submission* .

Govindjee, S. & E.P. Kasper. 1999. "Computational Aspects of One-Dimensional Shape Memory Alloy Modeling with Phase Diagrams." *Computer Methods in Applied Mechanics and Engineering* 171:309–326.

Gurtin, M.E. 1983. "Two Phase Deformations of Elastic Solids." *Archive for Rational Mechanics and Analysis* 84:1–29.

Gurtin, M.E. 1984. "On a Theory of Phase Transitions with Interfacial Energy." *Archive for Rational Mechanics and Analysis* 87:187–212.

Gurtin, M.E., J. Carr & M. Slemrod. 1984. "Structured Phase Transitions on a Finite Interval." *Archive for Rational Mechanics and Analysis* 86:317–351.

Huang, M. & L.C. Brinson. 1998. "A Multivariate Model for Single Crystal Shape Memory Alloy Behavior." *Journal of the Mechanics and Physics of Solids* 46:1379–1409.

Huang, W. 1999. "Yield Surfaces of Shape Memory Alloys and Their Applications." *Acta Metallurgica* 47:2769–2776.

Kohn, R.V. 1991. "The relaxation of a double well energy." *Continuum Mechanics and Thermodynamics* 3:193–236.

Luenberger, D.G. 1989. *Linear and Nonlinear Programming, Second Edition.* Addison-Wesley Publishing Company.

Mielke, A. & M.S. Kuczma & F. Theil. 1998. "Stress- and Strain-Induced Phase Transformations in Engineering Materials." *Preprint Nr. A10, IfAM, Universität Hannover.*

Nenno, S. & T. Saburi. 1981. "The Shape Memory Effect and Related Phenomena." *Proceedings of an International Conference on Solid Solid Phase Transformations* pp. 1455–1479.

Polak, E. 1997. *Optimization. Algorithms and Consistent Approximations.* Springer-Verlag.

Qidwai, M.A. & D.C. Lagoudas. 2000. "Numerical Implementation of a Shape Memory Alloy Thermomechanical Constitutive Model Using Return Mapping Algorithms." *International Journal for Numerical Methods in Engineering* 47:1123–1168.

Shield, T.W. 1995. "Orientation Dependence of the Pseudoelastic Behavior of Single Crystals of Cu-Al-Ni in Tension." *Journal of the Mechanics and Physics of Solids* 43:869–895.

Simo, J.C. & R.L. Taylor. 1986. "Consistent Tangent Operators for Rate Independent Elastoplasticity." *Computational Methods in Applied Mechanics and Engineering* 48:101–118.

Siredey, N., E. Patoor, M. Berveiller & A. Eberhardt. 1999. "Constitutive Equations for Polycrystalline Thermoelastic Shape Memory Alloys. Part I: Intergranular Interactions and Behavior of the Grain." *International Journal of Solids and Structures* 36:4289–4315.

Smyshlyaev, V.P. & J.R. Willis. 1999. "On the relaxation of a three-well energy." *Proceedings of the Royal Society of London A* 455:779–814.

Xiaochuang, Wu & T.J. Pence. 1998. "Two variant modeling of shape memory materials: unfolding a phase diagram triple point." *Journal of Intelligent Material Systems and Structures* 9:335–354.

Table 3. Approximate Properties for a Cubic-Orthorhombic Material

Reference Density	6448.1	kg/m^3
Young's Modulus	100.0×10^9	N/m
Poisson's Ratio	0.25	
Latent Heat of Transformation	6.6×10^3	J/kg
Heat capacity	4.0×10^2	J/(kg K)
Reference Temperature	277	K
Coefficient of Thermal Expansion	6.5×10^{-6}	1/K
Martensitic Bain Stretch	$\text{diag}\{1.0620, 0.9180, 1.0230\}$	

APPENDIX A. MATERIAL PROPERTIES

The purpose of this appendix is to specify the material properties employed in the simulations. A complete specification consists of the elastic moduli, the thermal expansion tensors, the reference density, the reference temperature, the latent heat of transformation, the heat capacity, the Bain strain tensors, and the orientation vectors of the parent lattice. Since it was assumed that the material was isotropic and has the same moduli for each variant, it is sufficient to specify the Young's modulus and Poisson's ratio for the moduli, and a single coefficient of thermal expansion for the thermal expansion tensors. With this in mind, Table 3 lists all of the properties with the exception of the global and martensitic orientation vectors which are discussed further below. The same set of properties were used for all of the examples, including the phase diagram computations.

The entry of Table 3 entitled Martensitic Bain Stretch describes the right stretch tensor associated with the phase change from austenite to a single variant of martensite in terms of a basis aligned along the martensitic crystal axes. Thus, material symmetry of the cubic parent lattice requires the existence of a six equivalent symmetry related lattice correspondent variants. Each of these may be described by specifying the six equivalent transformations from the Bain strain in the martensitic basis to the Bain strains in the parent (cubic crystal aligned) basis.

Such data has been reported for Cu-Al-Ni by Nenno & Saburi (1981) and is reproduced here in Table 4 for completeness. Additionally, the orientation of the parent lattice with respect to a global standard orthonormal basis aligned with the tension axis of the simulations of Section 5 as reported by Shield (1995) is given in Table 5. The data of the two tables allow one to compute the six Bain strains in the global basis as needed for the discrete implementation. This is accomplished simply by first transforming the Bain strain to the six orientations with respect parent basis, and then transforming again to the global basis. (It is also common that the results of the first step are presented in the literature in the form of the six Bain strains expressed in the parent lattice frame, see for example, Bhattacharya & Kohn (1996)). Here, the numbering of the variants matches that used by Shield (1995) to ease comparison of results. Explicitly, the computation of the Bain strains is given by $\boldsymbol{\varepsilon}^\alpha = \boldsymbol{Q}^T \boldsymbol{Q}^{\alpha T} \boldsymbol{\varepsilon}^o \boldsymbol{Q}^\alpha \boldsymbol{Q}$ where $\boldsymbol{Q}^\alpha$ are the tensors given in Table 4, $\boldsymbol{Q}$ is the rotation whose rows are $\boldsymbol{t}^1$, $\boldsymbol{t}^2$, and $\boldsymbol{t}^1 \times \boldsymbol{t}^2$, and $\boldsymbol{\varepsilon}^o$ is the small strain consistent with the data of Table 3.

Table 4. Lattice Correspondent Orientation Data.

Cubic $\leftrightarrow$ Orthorhombic								
$Q^{\alpha=5}$			$Q^{\alpha=6}$			$Q^{\alpha=1}$		
0	-1	0	0	-1	0	$\frac{1}{\sqrt{2}}$	0	$\frac{1}{\sqrt{2}}$
$\frac{1}{\sqrt{2}}$	0	$-\frac{1}{\sqrt{2}}$	$-\frac{1}{\sqrt{2}}$	0	$-\frac{1}{\sqrt{2}}$	0	-1	0
$\frac{1}{\sqrt{2}}$	0	$\frac{1}{\sqrt{2}}$	$\frac{1}{\sqrt{2}}$	0	$-\frac{1}{\sqrt{2}}$	$\frac{1}{\sqrt{2}}$	0	$-\frac{1}{\sqrt{2}}$
$Q^{\alpha=2}$			$Q^{\alpha=3}$			$Q^{\alpha=4}$		
$\frac{1}{\sqrt{2}}$	0	$-\frac{1}{\sqrt{2}}$	$\frac{1}{\sqrt{2}}$	0	$-\frac{1}{\sqrt{2}}$	$-\frac{1}{\sqrt{2}}$	0	$-\frac{1}{\sqrt{2}}$
0	-1	0	$\frac{1}{\sqrt{2}}$	0	$\frac{1}{\sqrt{2}}$	$\frac{1}{\sqrt{2}}$	0	$-\frac{1}{\sqrt{2}}$
$-\frac{1}{\sqrt{2}}$	0	$-\frac{1}{\sqrt{2}}$	0	-1	0	0	-1	0

Table 5. Global orientation vectors for the cubic lattice.

Run	Vector	Vector Components		
A1-T1b	t^1	0.925	-0.380	0.000
A1-T1b	t^2	0.380	0.925	0.000
A1-T2b	t^1	-0.447	0.707	0.548
A1-T2b	t^2	-0.447	-0.707	0.548
A1-T3b	t^1	-0.577	0.707	0.408
A1-T3b	t^2	-0.577	-0.707	0.408